Microseismicity Monitoring and Site Characterization With Distributed Acoustic Sensing (DAS): The Case of the Irpinia Fault System (Southern Italy)

A. Trabattoni, G. Festa, R. Longo, P. Bernard, G. Plantier, A. Zollo, A. Strollo

JGR Solid Earth

RESEARCH ARTICLE
10.1029/2022JB024529

Key Points:

- An active tectonic area was monitored by a new dedicated fiber-optic cable deployed in a dry lake near a major fault
- Recordings were dominated by highly amplified waves with slow apparent velocities
- Modeling suggests that distributed acoustic sensing is particularly sensitive to site effects whereas energy analysis enables magnitude estimation

Supporting Information:

Supporting Information may be found in the online version of this article.

Correspondence to:

A. Trabattoni,
alister.trabattoni@gmail.com

Citation:

Trabattoni, A., Festa, G., Longo, R., Bernard, P., Plantier, G., Zollo, A., & Strollo, A. (2022). Microseismicity monitoring and site characterization with distributed acoustic sensing (DAS): The case of the Irpinia fault system (Southern Italy). *Journal of Geophysical Research: Solid Earth*, *127*, e2022JB024529. https://doi.org/10.1029/2022JB024529

Received 12 APR 2022
Accepted 8 SEP 2022
Corrected 8 OCT 2022

This article was corrected on 8 OCT 2022. See the end of the full text for details.

Microseismicity Monitoring and Site Characterization With Distributed Acoustic Sensing (DAS): The Case of the Irpinia Fault System (Southern Italy)

A. Trabattoni[1,2,3], G. Festa[2], R. Longo[1,4], P. Bernard[3], G. Plantier[1,4], A. Zollo[2], and A. Strollo[5]

[1]Groupe Signal Image et Instrumentation (GSII), École Supérieure d'Électronique de l'Ouest (ESEO), Angers, France, [2]Università di Napoli Federico II, Complesso University Monte S. Angelo, Napels, Italy, [3]Université Paris Cité, Institut de physique du globe de Paris, CNRS, Paris, France, [4]Laboratoire d'Acoustique de l'Université du Mans (LAUM), Institut d'Acoustique—Graduate School (IA-GS), CNRS, Le Mans Université, Le Mans, France, [5]GFZ German Research Centre for Geosciences, Potsdam, Germany

Abstract This paper reports the first results obtained thanks to the installation of a dedicated one-km fiber-optic cable, integrated within the Irpinia Near Fault Observatory regional network in Southern Italy. The cable was installed in a dry lake, located near the active faults responsible for the M6.9 earthquake that occurred in 1980. A distributed acoustic sensing (DAS) interrogator was deployed over a period of 4 months and a half and allowed to record tens of local events. To model the seismic phases observed in the recordings, simple seismic refraction experiments were conducted along with analyses of earthquakes and numerical simulations. Results show that in this peculiar geological context, DAS is mainly sensitive to waves guided horizontally by the subsurface low-velocity layered structure of the site. This leads to considerable site amplification but also wavefront deformation and allows to detect local microearthquakes without any stacking or other array processing techniques. Magnitude estimation was performed using a dedicated amplitude correction process, along with detection threshold estimation. The benefit of using stacking of DAS channels for improving signal-to-noise ratio was also estimated.

Plain Language Summary A fiber-optic cable was buried near the fault responsible for the devastating earthquake that struck the Irpinia region (Southern Italy) in 1980. A specialized instrument, called distributed acoustic sensing (DAS) interrogator, was used to measure micrometric deformations of the cable due to small earthquakes regularly produced by the faults. The ground where the cable was installed is composed by stratified and very soft materials which trap and amplify seismic waves. Through analysis and modeling, we demonstrated that DAS is particularly sensitive to those effects because of its measuring principle. We showed that wave amplification allows to record small earthquakes otherwise impossible to detect and that their magnitude can be estimated if corrections are applied. We characterized the wave deformation process, a first important step to enable the use of conventional detection and location techniques and unleash the true potential of DAS deployments in geological context presenting soft materials.

1. Introduction

Recent developments of Near Fault Observatories in Europe are focused on dense observation systems to investigate the physical processes occurring along the faults, to track fluid migrations and to discover forcing mechanisms that may evolve into the nucleation of large earthquakes (Chiaraluce et al., 2022). To improve the detection of very small events on faults, seismic regional networks are now complemented with arrays of sensors (e.g., Ben-Zion et al., 2015) sometimes completed by temporary arrays to reveal peculiar features of the fault system (e.g., Bindi et al., 2021). Arrays exploit the spatial coherency of signals to decrease the completeness magnitude of seismic catalogs and improve event location.

In parallel, initially boosted by the oil and gas industry, the "distributed acoustic sensing" technology (DAS) has been developing very rapidly in seismology in recent years. DAS converts standard communications fiber into a linear or curvilinear array of discrete vibration sensors. This technology measures phase variations of Rayleigh backscattered laser impulses in standard (non-grating) fibers. This allows to recover the strain rate along the optic-fiber cable induced by seismic vibrations (Liu et al., 2017; Mestayer et al., 2011).

Because of this dense instrumental spatial coverage, DAS can potentially act as an improved array and accurately detect, classify and locate local or distant earthquakes, contribute to determine the geological structure crossed by the waves traveling from the source to the fiber, and possibly estimate source parameters (Lindsey et al., 2017). DAS also represents a precious tool to monitor other natural phenomena over long distances in harsh environments. It is particularly suited for monitoring volcano activities and landslides or for underwater applications and near fault submarine observatories as tsunamis early warning systems (Jousset et al., 2018; Lindsey et al., 2017; Wang et al., 2018).

A first difficulty linked to DAS deployments lies in the accurate fiber-optic cable geo-localization and in the estimation of the coupling with the ground for correct estimation of the wavefield amplitude. This is especially the case when already installed dark telecommunication fibers are used as these cables are encapsulated inside badly known sets of pipes. Fluctuations in space of the coupling with the ground can lead to important variations in the recorded amplitude (e.g., Sladen et al., 2019). To overcome this drawback, one solution is to use a dedicated direct-burial cable installation whose location can be accurately determined using a Differential Global Navigation Satellite System (DGNSS).

Another difficulty in the analysis of the observed seismic phases in DAS recording lies in the fact that DAS records the deformation along the cable instead of the 3D displacement of the ground. This may imply the selection of uncommon seismic phases and induce ambiguities in the attribution of wave types. In the case of an oceanic cable laying on sediments, it has been shown that Scholte waves dominate in the recordings (Lior et al., 2022; Spica et al., 2022) and that this has direct consequences on detection capabilities (Lior et al., 2021). Moreover, as DAS operates at high spatial resolution, small local structure variations of the soil can have a non-negligible impact on the observed wavefield. Eventually, to apply proper array processing algorithms, a good knowledge of the wave propagation pattern in the specific measurement site is required.

In this study we present a new DAS experiment using a dedicated fiber-optic cable deployed in a tectonically active region: the Irpinia normal fault area (Southern Italy). Because of the small size of the deployed fiber-optic cable, and the good coupling due to the choice of using a dedicated installation, this study focuses on a deep understanding of the DAS response at small scales to local microearthquakes.

This paper presents the installation and the signal acquisition in the context of the monitoring of the Irpinia tectonic area (Section 2). Typical recordings of local earthquakes is then shown, highlighting common features extracted from the measured wavefield (Section 3). To better explain the observed signals, a physical model of the deployment site is presented through the analysis of hammer shots and the picking of earthquakes phases along the fiber (Section 4). Numerical simulations performed to support the proposed model and interpret seismic phases are also described. In Section 5, the capacity of DAS to estimate the magnitude of events is evaluated by comparing DAS recordings to those of a nearby seismic station named COL3. Finally, conclusions and additional perspectives to complete the array processing techniques applied to DAS measurements are discussed (Section 6).

2. Experimental Setup

2.1. The Irpinia Site and the Near Fault Observatory

The Irpinia Near Fault Observatory (INFO) monitors the area that experienced the M 6.9, 1980 Irpinia earthquake, the strongest and most destructive seismic event of the last decades in Italy (Rovida et al., 2019). The present-day seismicity is mainly confined to the graben delimited by the main fault segments of the 1980 earthquake and is characterized by several swarm-like microearthquake sequences (Festa et al., 2021; Stabile et al., 2012). Velocity and attenuation tomographic images show an anomaly corresponding to earthquake locations (low vs., high vp-to-vs; high Qp), indicating the presence of fluids, eventually with a mixture brine-CO_2 and/or CH_4-CO_2 (Amoroso et al., 2014, 2017; Vassallo et al., 2016). The central sector of this area—the Monte Marzano region—where the DAS system and the fiber have been installed, is characterized by the largest release of seismic moment and small stress drops, as compared to the northern and southern sectors of the area (Picozzi et al., 2022).

To monitor the evolution of the seismicity the area is monitored by INFO, that operates the Irpinia Seismic Network (ISNet), a dense, high-dynamic range seismic network of 31 stations, covering an area of about 120×90 km^2 (Iannaccone et al., 2010). Each seismic station is equipped with a strong-motion accelerometer and

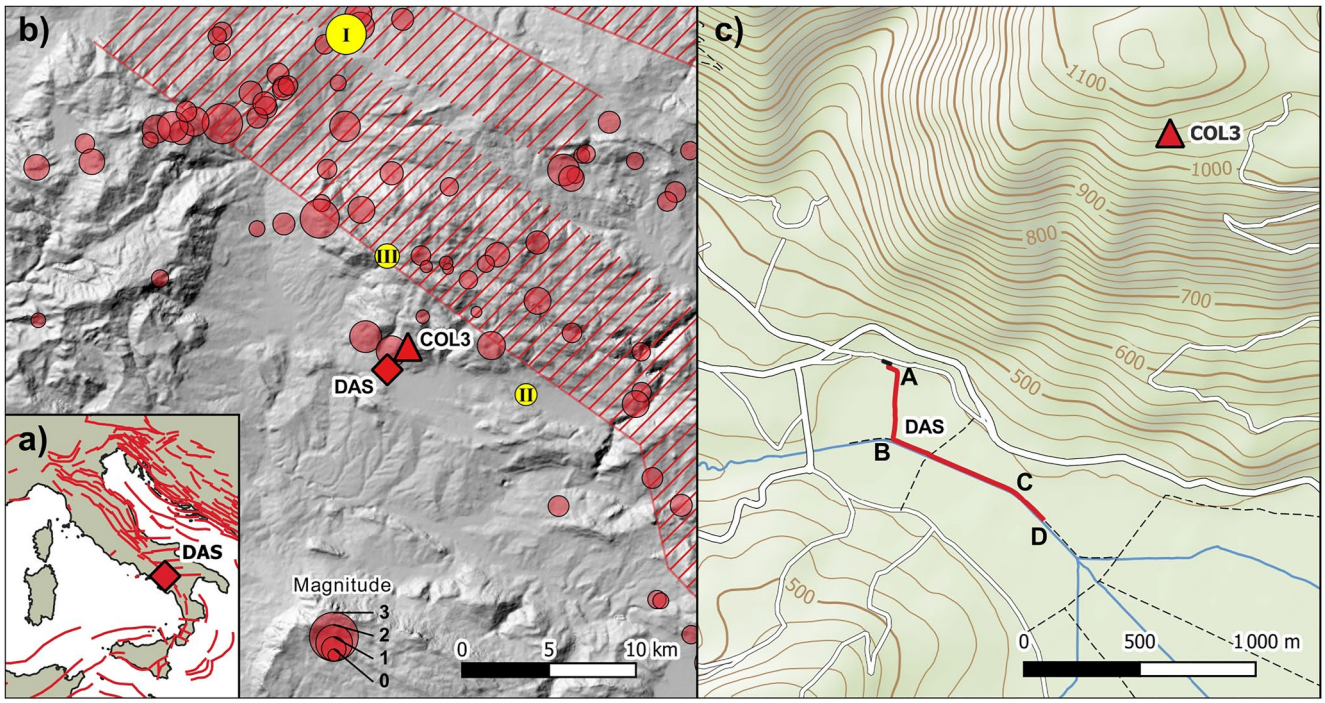

Figure 1. Distributed acoustic sensing (DAS) deployment in the Irpinia area. (a) Regional map with the experimental site (red diamond) and the major faults (red lines) taken from the European Database of Seismogenic Faults (Basili et al., 2013). (b) DAS deployment (red diamond) is located very closely to COL3 (red triangle), one of the stations of the Irpinia Seismic Network (ISNET) network. Both instruments are a few kilometers away from the faults that were activated by the M6.9 earthquake in 1980 (red hatched area). During the experiment, numerous local events have been detected by ISNET (red circles). Three events I, II, and III (yellow circles) were extensively analyzed in this study. (c) Topographic map of the area. The optic-fiber cable is buried in a dry lake while the COL3 station is situated on the top of a hill. A small water draining channel system (blue lines) allows to evacuate the water collected by the basin but does not produce notable noise as the water flow rate is low and not turbulent.

a weak-motion sensor (short-period velocimeter, broadband sensor or lower full-scale accelerometer) to record vibrations associated with earthquakes and ambient noise. Data and products of INFO are distributed through the EPOS data portal (https://www.ics-c.epos-eu.org) and the FRIDGE—Near Fault Gateway (https://fridge.ingv.it).

2.2. The DAS System and the Fiber Underground Installation

The fiber-optic cable was buried in a dry lake that is used for agriculture (Figure 1c). The dry lake is located 2 km south-west of COL3, a seismic station of ISNET located on the outcropping bedrock. A nearby school facility, made available by the local municipality, hosted the DAS interrogator (model: Febus A1-R DAS) along with a GPS antenna for time synchronization and a GSM antenna for real-time recovering of events detected by ISNET. A one-km dedicated optic-fiber cable was buried directly into the ground. According to literature, the type of optic-fiber cable does not really influence the signal quality (Dou et al., 2017; Papp et al., 2017) and a standard communication cable was purchased (Belden A/I-DQ(ZN)BH YE04689). The cable was a loose, gel-filled, 4 monomodal fiber with a dielectric sleeve. A geometry with mainly two sections was chosen to conciliate a big aperture, several geographical directions of the cable, and the constrains implied by the site configuration. Each section was labeled by markers located at their extremities (from A to D, see Figure 1c). On segment AB a one-m-deep trench was dug and then refilled using two excavators to go underneath a cultivated area. Subsequently, a shallower 30 cm deep trench was dug aside a dirt road. Every 20 m in average, markers providing the length of the cable were localized with DGNSS allowing to get the positioning of the cable with submeter accuracy. The deployment, greatly facilitated by the flat and soft nature of the ground, required 2 days of work in total.

The DAS interrogator was recording at nominal state from 2 September 2021 to 18 January 2022. The experiment lasted 138 days with a data coverage of 72%, due to instrumental failures (mainly software bugs). The following acquisition parameters were used: a gauge length of 4.8 m, a derivation time of 10 ms, a raw spatial resolution of 40 cm down sampled to 2.4 m and an raw sampling rate of 10 kHz (then increased to 20 kHz on 4 October 2021) down sampled to 200 Hz.

Table 1
Parameters of the Three Events Presented in Figure 1b Used to Illustrate the Present Study

Event	Origin time	Magnitude	Distance (km)	Depth (km)	Bearing
I	2021-10-03 04:22:31.63	2.3	19.6	8.0	3°W
II	2021-09-11 02:48:27.62	0.8	8.1	3.2	104°E
III	2021-09-23 05:04:47.41	1.0	6.6	3.2	4°E

Note. Distances and bearings are measured from the central B marker of the fiber.

3. Earthquake Recordings

Using the catalog provided by ISNET, seismic events that automatically triggered a detection at the COL3 station were used to extract portions of data where earthquake related signals should be observed on the DAS recordings. In the next paragraph we report the observed waveforms and results derived from dedicated processing such as spectrograms and Frequency-Wavenumber analysis (FK). Three events are used to illustrate this work (see Figures 1b and Table 1) and were chosen for their quality and for the range of distance/back azimuth origins. Several other examples are provided in the online supporting information file.

3.1. Waveforms

Events were analyzed using 2D time-offset representations (Figure 2, see also online Figure S1 in Supporting Information S1). Signal amplitude was

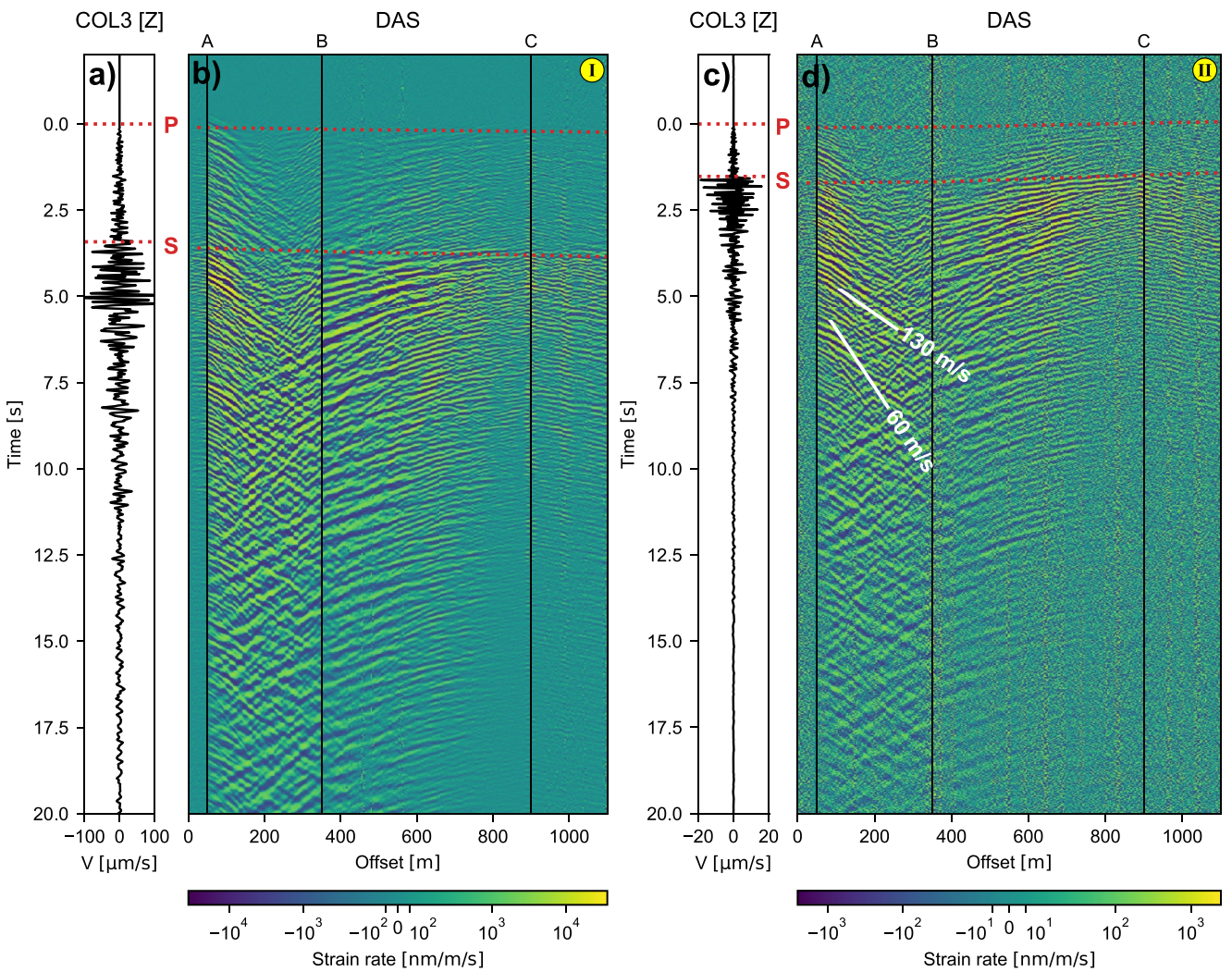

Figure 2. Recordings for events I and II. (a and c) COL3 vertical velocity (b and d) distributed acoustic sensing horizontal strain rate. Markers A, B, C, D correspond to the fiber position presented on Figure 1c. Strain rate is color-coded using a symmetric logarithmic law. The onset of the P and S wave trains are well identifiable, and correspond to the theoretical arrival time (red dashed lines). Both wave trains share similar patterns despite the fact that they come from almost orthogonal directions. However, observed signals propagate with an apparent velocity which is much slower than expected (oblique white lines for interpretation). Reverberation can be observed especially on the AB segment.

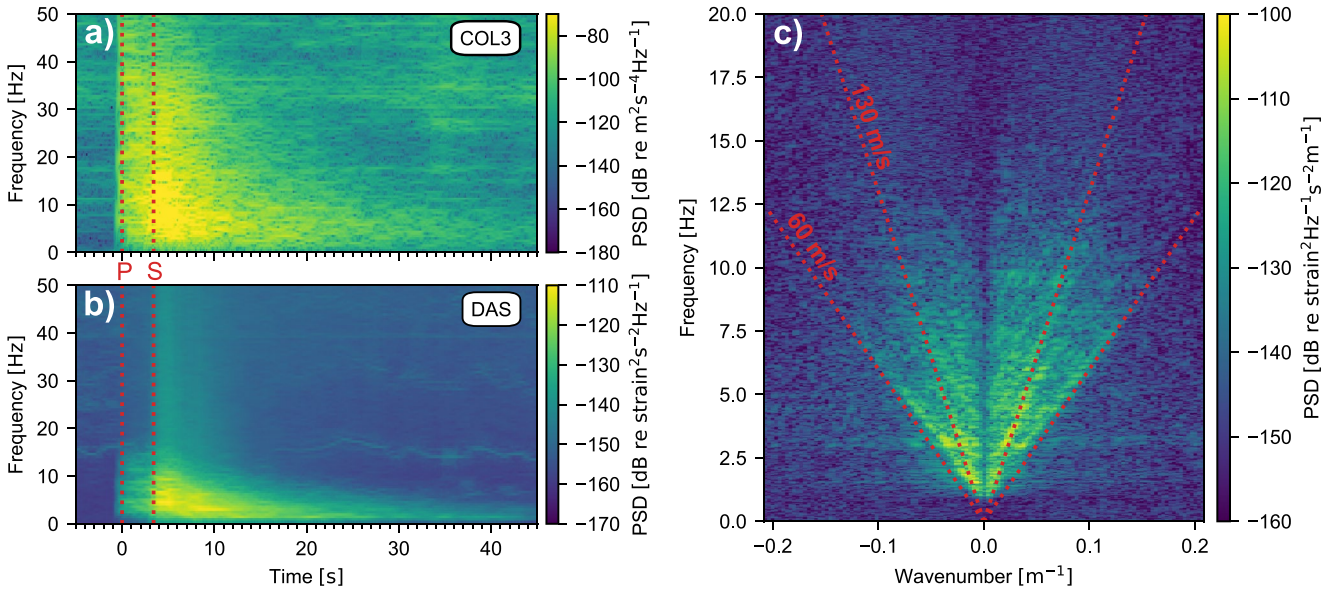

Figure 3. (a) Spectrogram of COL3 and (b) the power-averaged spectrogram along AB for event (I) P- and S-wave arrival picked on COL3 (red dashed-line) can be retrieved on the DAS. The S-wave arrival is clearly more energetic than the *P*-wave one. (c) FK analysis of the same data on the AB segment. Apparent velocities of 60 and 130 m/s (red dashed lines) clearly delimit FK features. Analyses of the BC segments are available online (Figure S2 in Supporting Information S1).

color-coded with compressed schemes using nonlinear mapping to better appreciate small transients associated with the first arrival. In these representations, the slope gives the apparent velocity along the fiber. Clear P and S arrivals can be observed on the DAS recordings. The arrivals time of the mentioned two phases correspond to those observed by COL3. However, looking carefully to each arrival at the 2D waveform structure in the time-offset representation, a more complex behavior can be observed:

1. While theoretical P and S arrivals along the cable predict the onset of the wave train, the observed wavefronts do not follow the expected arrival-time curve and instead show very low apparent velocities. In particular, the expected direct P-wave arrival—which is thoroughly used in standard array processing techniques to locate events—is not observed.
2. The P wave train and the S wave train, while corresponding to phases with different wave speeds, show very similar waveform patterns, the S arrival being only more energetic.
3. Waveforms related to events located at different distances, depths, and back azimuths also show very similar waveform patterns. Only the P to S time of arrival varies according to the distance of the event.

Looking more carefully at the waveform structure, we mainly observe slow waves with apparent velocities from 60 to 400 m/s. Those velocities are not consistent with shallow, near-surface regional P and S wave speeds, being estimated to be around 3,200 and 1,700 m/s, respectively (Matrullo et al., 2013), which should represent a lower limit for apparent velocities. On the segment AB, two main apparent velocities predominate (60 and 130 m/s). These two phases appear to be generated at the border of the dry lake, since the wavefronts show a common origin (point A in Figure 2) before separating and following their respective wave speed. The first arrival is composed of a less energetic phase with variable and higher apparent velocity (around 400 m/s). Reverberation appears to occur in the segment AB while this effect is less pronounced in the BC segment. All those observations suggest strong site effects.

3.2. Spectrogram and FK Representation

To further characterize the DAS response compared to COL3, a spectral analysis was conducted (Figures 3a and 3b). Comparing the averaged spectrogram of DAS on the AB segment with the spectrogram of COL3, it appears that the P and S arrivals are clearly visible on both recordings. The P to S contrast is more pronounced on DAS. According to measurements, most of the energy is located within the 1–15 Hz frequency range.

The FK analysis of the AB segment (Figure 3c) shows that a minimum apparent velocity of 60 m/s is observed and should correspond to the Rayleigh-wave velocity of the top layer of the dry lake. A strong low cutoff frequency

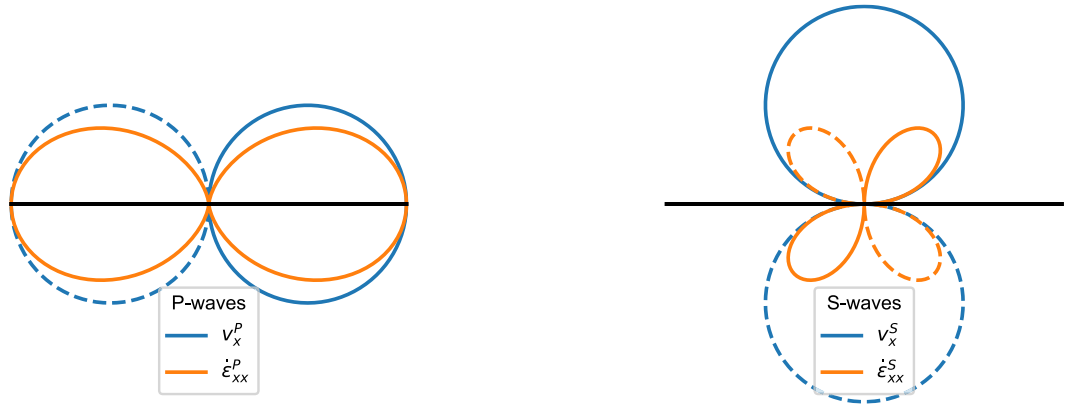

Figure 4. Distributed acoustic sensing and seismometer polarization patterns along the same direction (black line). Solid and dashed lines correspond respectively to positive and negative responses. (a) P-wave response. (b) S-wave response.

of about 1 Hz and interferences of higher apparent wave speed suggest that the dry lake acts as a stratified waveguide. Lack of high frequency could be explained by strong attenuation in the dry lake. The same analyses conducted on the BC segment (see online Figure S2 in Supporting Information S1) highlights similar spectral properties but with higher minimum apparent velocity, suggesting that the road is made of harder materials.

4. Waveform Simulations and Interpretations

To better understand the site effects linked to the dry lake structure, active seismic experiments and phase picking of earthquakes along the fiber-optic cable have been performed. This allowed to model the dry lake structure and develop full waveform simulations to better interpret DAS recordings. The following part of this study will focus on the AB segment for several reasons: (a) This segment is subject to more visible site effects. (b) Its direction makes an orthogonal section of the dry lake/nearby hill interface that plays a key role in the transmission of the observed phases (see later). It is also oriented in the minor axis of the basin favoring simplified 2D modeling. (c) Logistic reasons restricted the active experiments to this area.

4.1. DAS Theoretical Sensitivity

DAS measures the strain rate component $\dot{\varepsilon}_{xx}$ along the cable direction x, which is the spatial derivative of the ground motion v_x along that direction:

$$\dot{\varepsilon}_{xx} = \frac{\partial v_x}{\partial x} = jk_x v_x \tag{1}$$

Where j is the imaginary unit (using complex notation) and k_x is the apparent wavenumber along x. Thus, DAS signal is the quadrature of the along-cable velocity multiplied by the apparent wavenumber in that direction. This implies several difference between traditional seismic motion measurements and DAS deformation recordings:

1. The polarization pattern of DAS is given by the horizontal velocity pattern projected on the cable direction (Figure 4). For P-waves, DAS pattern is more directive than classical seismometers. For S-waves the pattern has a clover like shape with nulls along and orthogonal to the cable, and maximum response at 45° (Martin et al., 2018; Papp et al., 2017).
2. DAS response is inversely proportional to the wavelength, smaller wavelengths are better recorded (Wang et al., 2018). In case of site amplification due to superficial low velocity zone DAS is affected twice as much than with a traditional horizontal velocity measurement, since wavelength is shortened when the wave enters low-velocity layers, further increasing DAS sensibility.

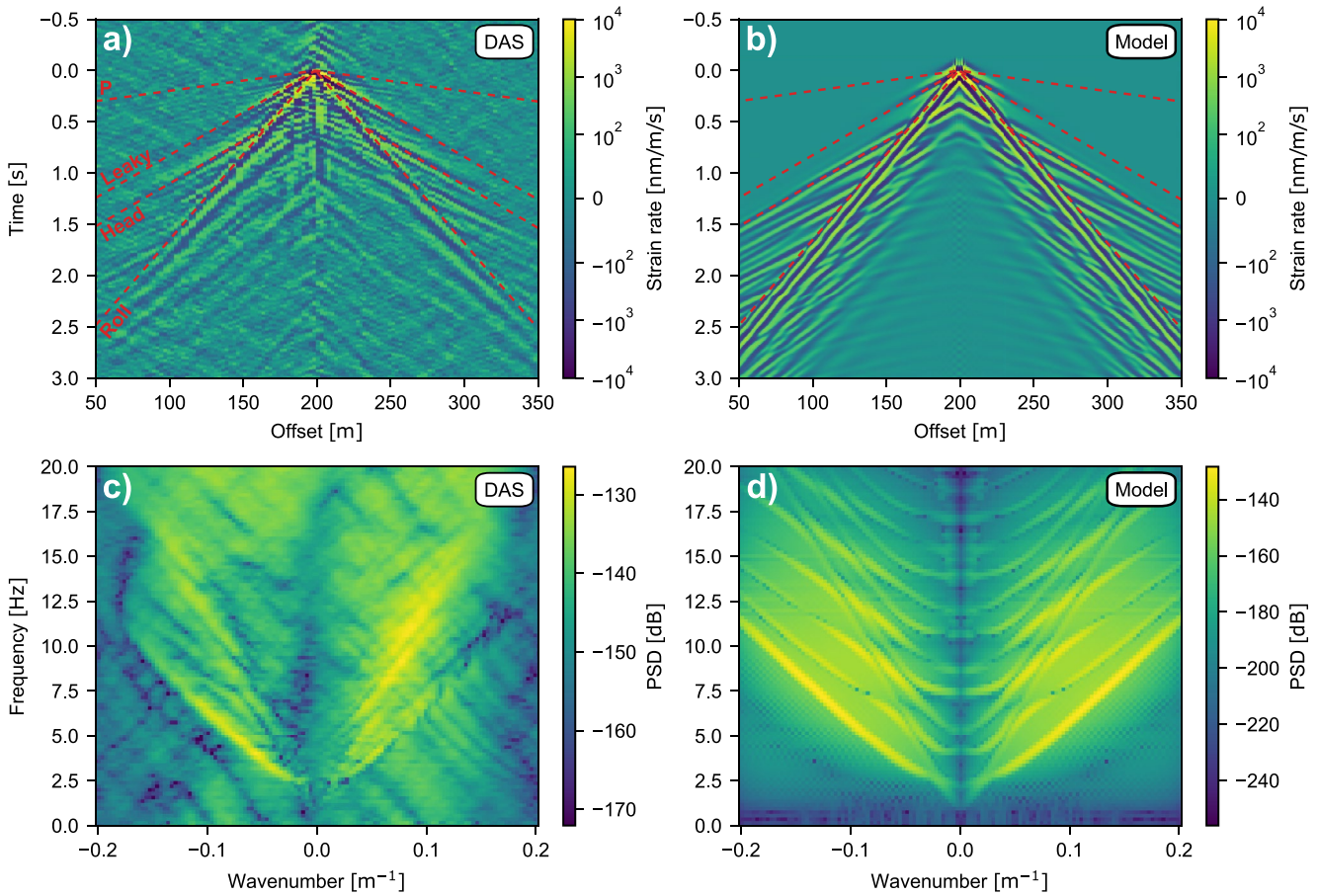

Figure 5. Active seismic refraction experiment. (a) Stack of three hammer-shots located at the middle of the AB segment. Red dashed lines show theoretical arrival times for the different identified phases. (b) Simulation of the hammer shot. Much more reverberation can be observed, probably due to the lack of attenuation in the simulation and the simplicity of the model. Yet the main features superimpose well. FK analysis of real data (c) and simulated data (d) also share similar features. Other hammer-shots can be seen online (Figure S3 in Supporting Information S1).

4.2. Active Source Refraction Experiment

Shots were hammered on 15 evenly spaced locations along the first 150 m half of the AB segment (Figure 5a and online Figure S3 in Supporting Information S1). The analysis of common-shot gathers allowed to identify four main phases:

1. A first very faint arrival that can be interpreted as the P front horizontally traveling at roughly 500 m/s in the most superficial layer (Noted P in Figure 5a). Other refracted or reflected P-waves phases must have higher apparent speed (depending on their incidence) but are not observed by the DAS.
2. A second arrival, interpreted as the leaky front, traveling at 120 m/s in the same layer as well (noted Leaky in Figure 5a). Leaky waves are evanescent Rayleigh waves that are observable in media of high P to S wave-speed ratio and that travel nearly twice as fast as S waves (Gao et al., 2014).
3. A Rayleigh wave arrival traveling at roughly the speed of S waves of 60 m/s in the most superficial layer (noted Roll in Figure 5a).
4. A first conical (or head) S wavefront, traveling at 130 m/s in an underneath layer (Noted Head in Figure 5a).

Using classical seismic refraction methods, a profile of the first layer could be constructed for the first half of the AB section (Figure 7). The layer is mostly 10 m thick, except near the dry lake border where the interface rises to the surface. The P-wave velocity of the second layer along with its thickness could not be constrained from observations. The presence of water wells may suggest that this layer is water saturated and consequently the speed of P-waves was assumed to be 1500 m/s. The depth of the second layer was determined by picking the first phase of earthquakes and will be described in the next section. As no other clear conical fronts could be

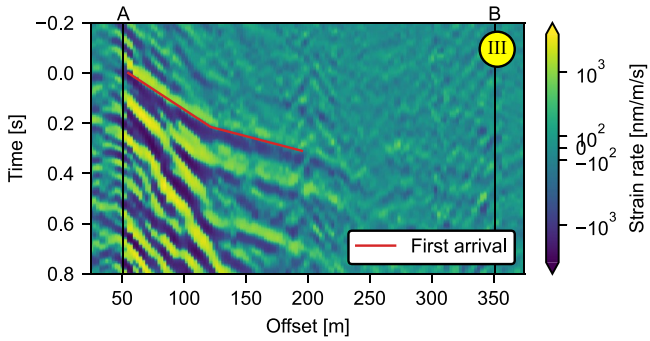

Figure 6. Picking of the first arrival (red line) on the first half of the AB section for the S onset of event III. In first approximation, this gives the difference of travel time to cross all the sedimentary layers at each offset. P onset of events I and II can be seen online (Figure S4 in Supporting Information S1).

observed, it was supposed that below the water saturated zone, there is the bedrock layer. Indeed, this layer, due to its solid matrix, mainly supports high speed propagation modes that are difficult to measure by means of the DAS. Physical parameters of the bedrock layer were taken from the regional study of (Matrullo et al., 2013). All parameters are reported in Table 2.

To validate the proposed interpretation, a full-waveform simulation of the shot located in the middle of the AB segment using the estimated parameters was developed (Figure 5b). As the structure of the dry lake is flat near the middle of the AB segment, a 1D model was employed with the axisymmetric mode proposed in SPECFEM2D (Bottero et al., 2016). For simplicity sake, attenuation effects have not been considered. A vertical force, represented by a 7 Hz Ricker impulse, was applied at the surface of the horizontally stratified medium composed by the layers reported in Table 2. The horizontal velocity on the surface was evenly computed using the same spatial resolution than the DAS measurements. Afterward, the horizontal, along fiber, strain rate was computed by differentiation of each pair of spatial points located at both ends of a gauge length (Daley et al., 2016). Both real and simulated data share the same main phases described earlier in this section. Moreover, FK analyses share several branches and splitting features. More reverberation and propagation branches are observed in the simulations, probably because of the lack of attenuation and of the simplified horizontally layered 1D model used. This suggests that important attenuation and/or scattering must occur in the shallow unconsolidated layers.

4.3. Seismic Transmission Profile Interpretation

To complete the information provided by the refraction experiment, major events aligned with the AB axis with clear first arrival of either P or S onset were used (Figure 6 and online Figure S4 in Supporting Information S1). The arrival time of this phase varies along the cable because of the variation of: (a) the arrival time at the bedrock basement and (b) the time taken by the transmitted S-wave to propagate across the shallow layers which thickness varies laterally according to the fiber location. In this study, the first term can be considered negligible at a first-order approximation. This is due to the high S-wave speed contrast between the dry lake and the bedrock, the relatively small size of the deployed cable and the actual thickness of the dry lake. Indeed, P and S waves travel faster along the bedrock-sediments interface than in the dry lake, resulting in an almost instantaneous excitation of the whole base of the basin. Moreover, because of the high diminution of S wave speed in the dry lake, the seismic rays bend almost vertically. Consequently, the first arrival time represents a good proxy of the variations of the overall basin thickness.

An average time difference of arrival relative to point A was manually picked comparing different events (Figure 6 and online Figure S4 in Supporting Information S1). The thickness of the second layer was supposed to be null at the beginning of the section, which is compatible with an horizontally stratified geometry. The contribution of the first layer estimated from the seismic refraction experiment was removed from the overall delay to isolate the contribution of the second layer. The S-wave speed of the second layer being also constrained by the seismic refraction experiment, the thickness of the second layer could be determined. Details on this procedure can be

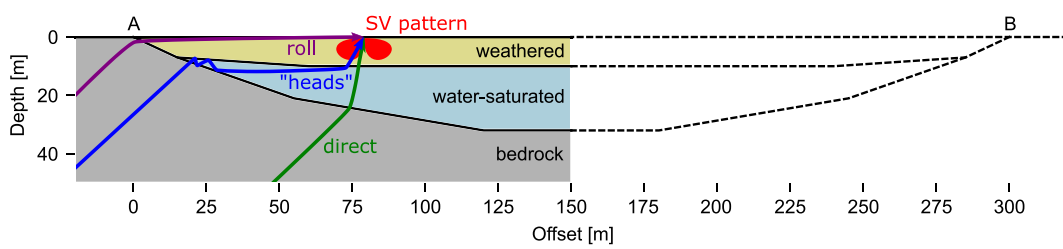

Figure 7. Model of the first half of the AB section. The combined use of the active refraction experiment along with the picking of the first arrival allowed to build this model. To run the simulation, the basin has been completed by symmetry. Three main phases are observed (colored lines) with amplitudes partly linked to the polarization pattern response of distributed acoustic sensing (SV vertical pattern illustrated in red) but also to their apparent horizontal wavenumber.

Table 2
Physical Parameters Recovered From the Active Seismic Refraction Experiment and From Earthquake Wave-Front Picking for the First Half of the AB Segment

Layer	h (m)	ρ (kg/m^3)	V_P (m/s)	V_S (m/s)
Weathered	0–10	1,500	500	60
Water saturated	0–20	2,000	1,500	130
Bedrock	∞	2,720	3,250	1,730

Note. Here, h is the thickness that evolves along the AB segment, ρ is the density and V_P and V_S the P- and S-wave speeds.

seen online (Figure S5 in Supporting Information S1). This completed the modeling of the first half of the AB segment (Figure 7).

4.4. Event Modeling

To support the reconstructed model, full waveform simulation of an event has been conducted (Figure 8). The model was completed by symmetry (Figure 7) for several reasons: (a) it simplified the numerical boundary conditions; (b) it allowed to run the simulation on a segment with the same size than the AB segment; and (c) obtained results ended up being close to observation, suggesting that the subsurface of the AB segment has a similar closed basin structure. Indeed at point B, the end of the fields along with the presence of a deep water channel suggest strong geological variations of the subsurface.

An incident 40° plane P-wave was simulated by using SPECFEM2D codes (Tromp et al., 2008). This value is characteristic of an incidence angle obtained by ray-tracing through the regional 1D model for events situated a few kilometers away. The use of an incident S-wave led to very similar results, highlighting the fact that, in both cases, an S-wave is simultaneously generated at the base of the whole basin either by refraction for S incidence or by P to S conversion for P incidence. This might also explain the increased contrast observed on DAS between the P and the S wave train because P to S conversion is expected to be less efficient than S-wave transmission. A 5 Hz Ricker source was used. To measure the site effect amplification, a similar simulation was implemented using a homogeneous half space with the same properties of the bedrock. This allowed to express the simulated waveform as a fraction of the amplitude obtained without the basin structure. Basin amplification factors above 10 in velocity and 100 in strain rate were obtained for certain phases. This highlights the fact that well-known amplification effects due to a decrease of the S-wave velocity further affect strain rate measurement due to the instrumental response of DAS, more sensitive to slower waves.

An additional key point of the presented simulation is to better understand the origin of the observed phases. The relative amplitudes of the different phases are mainly due to the polarization pattern of DAS. DAS is not sensitive to SV waves traveling close to horizontal/vertical directions. The mainly visible phases are:

1. "Direct" SV waves that cross the two layers with a given, non-null angle. Those are enhanced close to the edge of the dry lake, where the slope of the interfaces is greater and imply a deviation of the ray from the vertical.
2. "Conical-like waves" that enter from the tips of the basin, traveling almost horizontally in the second layer and finally refracting toward the surface with an angle close to the critical angle of SV waves (an angle the DAS is particularly sensitive to).

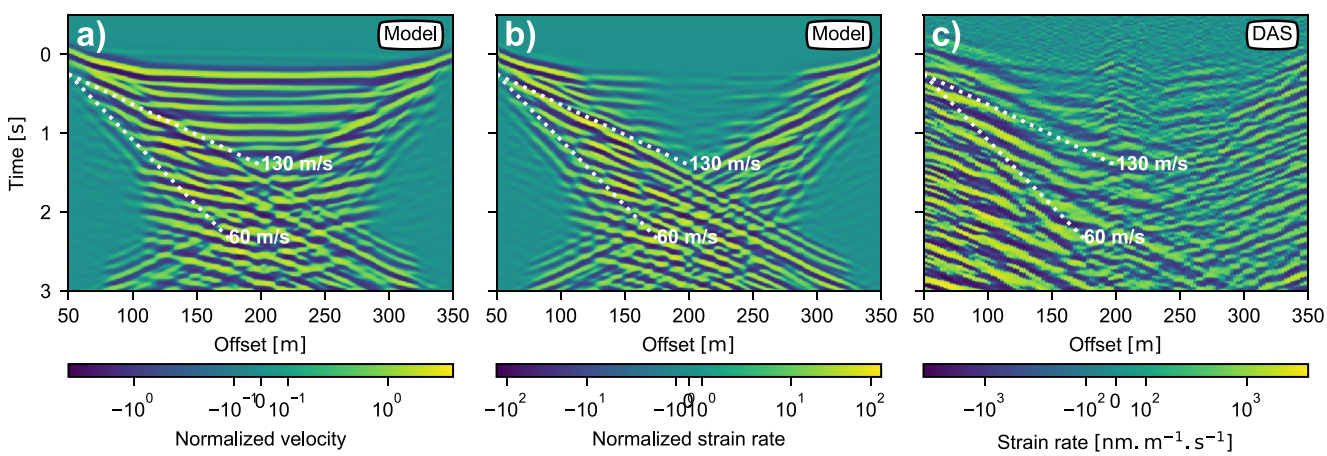

Figure 8. Event simulation with 40° incident P-waves for the AB section as described in Figure 7. (a) Velocity waveforms and (b) Strain rate waveforms both normalized by the maximum amplitude obtained from a simulation with only a flat bedrock layer. Amplification of a factor ∼10 is observed for the velocity and ∼100 for the strain rate. Three main phases shown on Figure 7 are observed. (c) Zoom on the corresponding time-offset region for the event I from Figure 2b. Main features present in the simulations can be observed. Because the earthquake source time function is not just an impulse, and because of the reverberation due to unmodeled velocity heterogeneities, continuous waves are observed.

3. Rayleigh waves, generated at the borders of the dry lake and propagating along the surface whose DAS is sensible to. The deepest the fiber-optic cable is buried, the less DAS is sensitive to Rayleigh waves.

From this analysis, it appears that most of the energy captured by the DAS is composed of horizontally guided waves. This can be seen in the various FK figures, where clear cutoff frequencies can be observed, corresponding to the maximum wavelengths the waveguide supports.

5. Microearthquake Detection Capabilities

The goal of a regional network of sensors is to detect and locate events with the minimum achievable detection threshold. In this part, we investigate the capabilities of DAS both in term of magnitude estimation and of catalog completeness. We also discuss the expected improvements that array processing techniques should allow.

5.1. Magnitude Estimation

To evaluate the capability of DAS to measure event magnitudes, amplitude comparisons between the extensively studied first half of the AB section and the nearby COL3 station of the INFO network has been studied. To compare both instruments in terms of amplitude, the average energy density measured on a time window of 6 s around the S-wave onset was computed for each event (from $t_1 = t_S - 1$ s to $t_2 = t_S + 5$ s; t_S being the S-wave time of arrival given by the INFO data set for the COL3 station). Both DAS and COL3 signals were filtered between 1 and 20 Hz, a frequency content where both sensors had good sensitivity to events. Because COL3 measured velocity while DAS measured strain rate, different computation methods were employed to make these different measurements comparable. At the COL3 station, we estimated w_k, the total (using the three velocity components v_x, v_y, and v_z) time average of the kinetic energy density:

$$w_k = \frac{1}{2}\rho \left\langle v^2(t) \right\rangle = \frac{1}{2}\rho \frac{1}{t_2 - t_1} \int_{t_1}^{t_2} |v_x^2(t) + v_y^2(t) + v_z^2(t)| dt \tag{2}$$

Here ρ is the density of the bedrock layer (see Table 2).

The first half of the AB section of DAS was employed to derive w_e, the horizontal component along the fiber of the time average of the elastic (or potential) energy density:

$$w_e = \frac{1}{2}(\lambda + 2\mu) \left\langle \varepsilon_{xx}^2(t) \right\rangle = \frac{1}{2}\rho c_P^2 \frac{1}{t_2 - t_1} \int_{t_1}^{t_2} \left| \int_{t_1}^{t} \dot{\varepsilon}_{xx}(\tau) d\tau \right|^2 dt \tag{3}$$

Here λ and μ are the Lamé coefficients while ρ is density and c_P is the P-wave speed of the weathered layer (see Table 2).

The above formula requires a temporal integration to transform the strain rate measured by DAS into strain. To filter uncorrelated noise present in DAS measurements, the energy estimation was performed on every channel of the first half of the AB section and the median of all the results was retained.

To differentiate events hidden in noise from other events, a rough signal to noise (SNR) estimation was performed as following. To estimate the ambient and instrumental noise w_e^{before}, the method used to estimate the elastic energy density of the S wave train w_e^{event} was reused on the time interval preceding the event (from $t_1 = t_P - 7$ s to $t_2 = t_P - 1$ s; t_P being the P-wave time of arrival). Because the power measured on the S wave train window also includes ambient/instrumental noise, SNR was estimated as:

$$\text{SNR} = \frac{w_e^{\text{event}} - w_e^{\text{before}}}{w_e^{\text{before}}} \tag{4}$$

Events with SNR <2 were estimated as not detected by the DAS. As detections from COL3 were initially used to construct the event data set, the number of events detected by the DAS but not by COL3 could not be estimated. Yet, the events detected by the DAS with lowest amplitude presented a level one order of magnitude larger than the lowest event detected by COL3. This highlights the fact that a one-channel DAS has one order of magnitude lower SNR than COL3 (with the parameters and the interrogator used in this study).

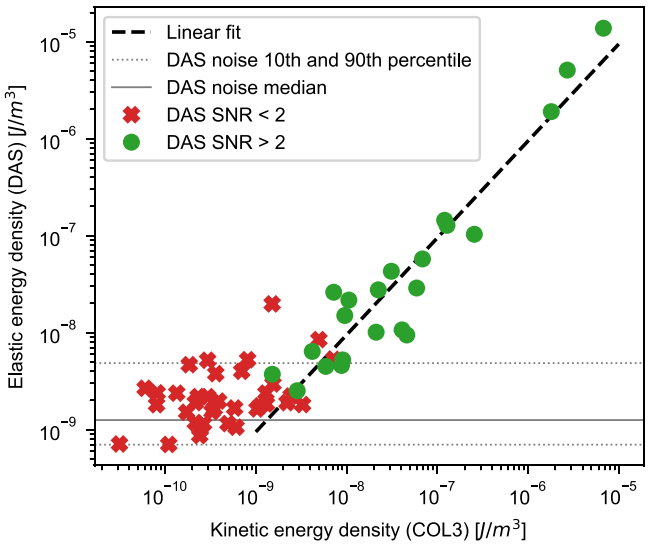

Figure 9. Power comparison of the S phase between the first half of the AB segment of distributed acoustic sensing and COL3 seismic station.

Using events detected both by the DAS and COL3, a clear linear correlation (in log scale) of the computed powers can be observed (Figure 9). When performing a linear fit, using events with SNR >2, we found that the slope is (0.99 ± 0.08), this value being compatible with one. This indicates that the two quantities are linearly related and are thus unbiased proxies for the energy propagating with seismic waves.

When fixing the slope to 1, the relation between DAS and COL3 could be described as: $w_e = a w_k$ where $a = 0.97 \pm 0.11$. Energy equipartition between kinetic and elastic contributions is expected locally. But in this case measurements are not co-located, making direct comparison not relevant. While amplification effect showed by simulations suggested that $w_e > w_k$, several factors limits this interpretation: (a) DAS only measures one component of the elastic tensor. (b) Physical parameters are not well constrained, some of them coming from regional models. (c) No proper calibration of DAS instrument nor cable coupling with ground was performed.

Yet, through a simple calibration procedure, the elastic energy density recorded at DAS can be converted into kinetic energy density recorded at COL3, allowing to use traditional magnitude estimation technics.

5.2. Detection Level

To evaluate the detection threshold of the fiber, a similar approach based on the detection criterion $\mathrm{SNR}^d = 2$ was adopted. The statistics of the DAS ambient noise were estimated by computing the elastic power density for all available 6 s windows through the whole data set (median, 10th and 90th percentiles are reported in Figure 9). The 90th percentile $w_e^{90\%}$ of this DAS noise distribution almost separates the events detected and not detected by the fiber. An event must reach a power of $w_e^d = \mathrm{SNR}^d \times w_e^{90\%}$ to be detected with a probability of 90%. This elastic power was translated into a kinetic power using the fit computed earlier (Figure 9). We thus computed the radiated energy E_r^d using the formula from Boatwright and Fletcher (1984):

$$E_r^d = 8\pi c_s^m R^2 E_k^d \tag{5}$$

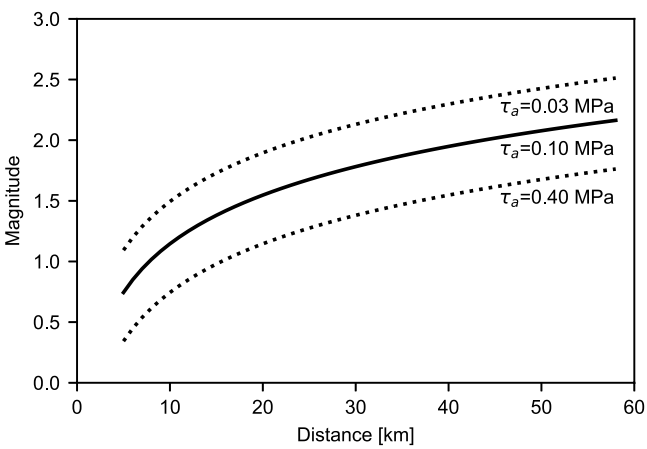

Figure 10. Magnitude detection threshold (with probability 90% at SNR = 2) as a function of the distance, for three values of the apparent stress. These values represent the median and 68.8% confidence limits of the apparent stress values for the Irpinia region (Zollo et al., 2014).

where c_s^m is an average value for source-receiver S wave speed, R is the distance and $E_k^d = (t_2 - t_1)\, w_k^d$ is the integrated kinetic energy density. We used the same shear modulus as in Zollo et al. (2014) $\mu = 3.3 \cdot 10^{10}$Pa, yielding $c_s^m = \sqrt{\mu/\rho}$, and the average S-wave radiation pattern contribution as described in Boatwright and Fletcher (1984). We finally converted the radiated energy into seismic moment M_0^d according to Wyss (1970):

$$M_0^d = \frac{\mu}{\tau_a} E_r^d \tag{6}$$

where τ_a is the apparent stress, and the seismic moment into the moment magnitude M_W^d using the Hanks and Kanamori (1979) formula: $\log M_0^d = 1.5\, M_W^d + 9.1$. Values for the apparent stress were taken from Zollo et al. (2014) which reported a median value of 0.1 MPa value for the Irpinia region with [0.03–0.4 MPa] as 68.8% confidence interval. This allowed to compute the magnitude detection threshold of the fiber, in function of the distance R of the event and its apparent stress τ_a (Figure 10).

The proposed model reports detection thresholds of M1.5 at 20 km and M1.9 at 40 km, which is coherent with observations. The variability of the apparent stress implies a variability of ±0.3 magnitude. We note that this estimation is conservative. When using the median value of the noise instead of the 90th

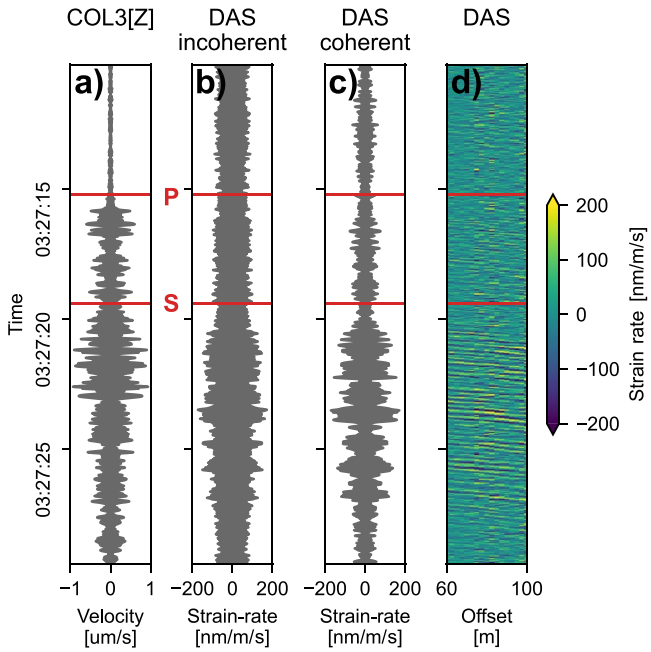

Figure 11. Noise reduction by stacking the first 16 channels of distributed acoustic sensing (DAS) using the most energetic apparent velocity. (a) Envelope of COL3 trace for an event with DAS SNR below 2. The event occurred the 9 September 2021 at 03:27:10 with magnitude M1.0, distance 27.7 km and depth 12.1 km. (b) Incoherent stack of the envelopes of the 16 channels. The noise level is about 100 nm/m. (c) Coherent stacking computed by delaying each trace according to an apparent velocity of 170 m/s. Noise level is lowered to 40 nm/m while the *S* arrival now clearly emerges. (d) DAS 16 first channels. Coherent wavefronts of the S arrival are visible.

percentile, detection thresholds of M1.1 at 20 km and M1.5 at 40 are obtained instead.

5.3. Noise Level Reduction by Stacking

Because DAS mainly records horizontally guided waves, a complete 3D understanding of the wave propagation should be required to better apply array processing techniques such as beamforming. Consequently, a SNR (in units of power) improvement ideally proportional to the number of channels could be achieved. While this approach has not been realized in the present study, results in that direction are presented here. Beamforming on the first 16 channels (about 40 m) using the apparent velocity that optimized the stacking (170 m/s) have been computed (Figure 11).

While a noise reduction factor of 4 (in amplitude) was expected (estimated before the P arrival), only 2.5 of reduction could be obtained. This suggests that ambient and instrumental noise recorded by the different channels are not completely uncorrelated. The inter-channel distance was half the gauge length and was also smaller than half the wavelength of signals of interest. The equivalent number of statistical independent channels can be empirically estimated by dividing the number of channels by $4^2/2.5^2 = 2.6$. For a 1 km long cable (with ∼400 channels at a spatial resolution of 2.4 m), the noise amplitude level could be lowered by about one order of magnitude. In that case, the expected detection level should be comparable to the one of the COL3 station. Deployments with larger spatial extent should allow to go even lower. Progress in term of instrumental noise in the field of DAS interrogator are also expected to improve the SNR in the medium term as this technology is still under development.

6. Conclusion and Perspectives

In this study, a dedicated 1 km fiber-optic cable has been deployed in a dry lake in the Irpinia tectonic area. From active refraction experiments and phase picking of earthquakes, a propagation model of the basin has been constructed and supported by full waveform simulations. In this survey, it is shown that DAS is only sensible to slow S waves arriving to the surface with an oblique angle of incidence (not vertical nor horizontal) and to Rayleigh waves. In particular, the first P arrival is completely unobserved. We interpret this finding as a result of the basin configuration and of the presence of slow superficial layers of unconsolidated materials, that bend vertically the seismic rays associated with direct arrivals from the source. Horizontal fibers show larger sensitivity to S waves than to the P waves (Ajo-Franklin et al., 2019) and to slower rather than faster waves (Lior et al., 2021). Similar findings have been retrieved for off-shore fibers installed in shallow submarine sedimentary layers, where records are dominated by Sholte waves (Sladen et al., 2019). For other surveys, where the ray does not impinge vertically below the surface, the P wave can be clearly recognized and in some cases, the SNR for the P wave on the DAS overcomes the value measured on colocated geophones (Piana Agostinetti et al., 2022; Wang et al., 2018).

Since in sedimentary areas, the most energetic recorded phases correspond to phases produced at the edge of the basin and guided horizontally, it implies strong 3D effects but also strong site amplification, allowing to record small events that would otherwise be impossible to measure with DAS (e.g., in a bedrock scenario).

By comparing amplitudes of signals measured at a nearby seismic station, event magnitude could be recovered from DAS recordings. While the SNR of single DAS channels was one order of magnitude lower than a traditional seismic station, stacking on small segments of DAS optic-fiber cable allowed to improve the SNR. Stacking along the whole one-km optic-fiber cable should allow to reach comparable detection threshold performances than with using a traditional seismic station.

In perspective, because body waves arriving to the dry lake travel faster than waves traveling inside the dry lake, they act at first order as an instantaneous excitation applied at the interface between the bedrock and the dry lake. This effect is more evident for near vertical incidence below the interface and in the deeper areas of the basin (e.g., at the middle of the AB segment), resulting into the fact that most events share the same propagation patterns and standard array processing techniques cannot be applied as is. Future processing techniques must be developed to analyze residual phase mismatches between events coming from different directions to individuate the source back azimuth. Through wave pattern characterization, this study is a first step in that direction. We expect those results to be generalized to most fiber-optic cable deployments not directly in contact with the bedrock. Also, this experiment creates the conditions to continue similar experiments within the INFO network within different site configurations, or experimenting with different DAS systems taking advantage of the well-known setup of the ad-hoc deployed cable.

Data Availability Statement

Data and codes necessary to reproduce the results presented in this paper are available on GitHub (https://github.com/atrabattoni/irpinia_monitoring_with_das—https://doi.org/10.5281/zenodo.7027780). Data related to the Irpinia Near-Fault Observatory (INFO) is available on the Irpinia seismic network infrastructure (ISNet: http://isnet.unina.it). The complete DAS data set is available on request. Please contact the corresponding author.

Acknowledgments
This work is linked to the IRPIDAS project, funded by Wise Professional Electronics program within the framework of the international call. This work has been conducted in collaboration with the GSII-LAUM group (Angers-Le Mans, France), the IPGP seismology group (Paris, France) and the RISSC lab, the Seismology Laboratory from the University of Naples (Italy). We are grateful to the municipality of Colliano, Giuseppe Scaglione and the major Adriano Goffredo for administrative and logistic support for fiber installation and DAS operation which included the provision of excavators; the municipality of Palomonte for administrative support; and the land tenants for their allowance to deploy the fiber. We also kindly thank Giuseppe Cappelli for his help in the preliminary analysis of the present study. Numerical computations were performed on the S-CAPAD/DANTE platform, IPGP, France.

References

Ajo-Franklin, J. B., Dou, S., Lindsey, N. J., Monga, I., Tracy, C., Robertson, M., et al. (2019). Distributed acoustic sensing using dark fiber for near-surface characterization and broadband seismic event detection. *Scientific Reports*, *9*(1), 1328. https://doi.org/10.1038/s41598-018-36675-8

Amoroso, O., Ascione, A., Mazzoli, S., Virieux, J., & Zollo, A. (2014). Seismic imaging of a fluid storage in the actively extending Apennine mountain belt, southern Italy. *Geophysical Research Letters*, *41*(11), 3802–3809. https://doi.org/10.1002/2014GL060070

Amoroso, O., Russo, G., De Landro, G., Zollo, A., Garambois, S., Mazzoli, S., et al. (2017). From velocity and attenuation tomography to rock physical modeling: Inferences on fluid-driven earthquake processes at the Irpinia fault system in southern Italy: From Seismic Tomography to Rock Modeling. *Geophysical Research Letters*, *44*(13), 6752–6760. https://doi.org/10.1002/2016GL072346

Basili, R., Kastelic, V., Demircioglu, M. B., Garcia Moreno, D., Nemser, E. S., Petricca, P., et al. (2013). European Database of Seismogenic Faults (EDSF). Istituto Nazionale di Geofisica e Vulcanologia (INGV). https://doi.org/10.6092/INGV.IT-SHARE-EDSF

Ben-Zion, Y., Vernon, F. L., Ozakin, Y., Zigone, D., Ross, Z. E., Meng, H., et al. (2015). Basic data features and results from a spatially dense seismic array on the San Jacinto fault zone. *Geophysical Journal International*, *202*(1), 370–380. https://doi.org/10.1093/gji/ggv142

Bindi, D., Cotton, F., Picozzi, M., & Zollo, A. (2021). *The Irpinia seismic array*. GFZ Data Services Other/Seismic Network. https://doi.org/10.14470/MX7576871994

Boatwright, J., & Fletcher, J. B. (1984). The partition of radiated energy between *P* and *S* waves. *Bulletin of the Seismological Society of America*, *74*(2), 361–376. https://doi.org/10.1785/BSSA0740020361

Bottero, A., Cristini, P., Komatitsch, D., & Asch, M. (2016). An axisymmetric time-domain spectral-element method for full-wave simulations: Application to ocean acoustics. *Journal of the Acoustical Society of America*, *140*(5), 3520–3530. https://doi.org/10.1121/1.4965964

Chiaraluce, L., Festa, G., Bernard, P., Caracausi, A., Carluccio, I., Clinton, J., et al. (2022). The near fault observatory community in Europe: A new resource for faulting and hazard studies. *Annals of Geophysics*, *65*(3), DM316. https://doi.org/10.4401/ag-8778

Daley, T. M., Miller, D. E., Dodds, K., Cook, P., & Freifeld, B. M. (2016). Field testing of modular borehole monitoring with simultaneous distributed acoustic sensing and geophone vertical seismic profiles at Citronelle, Alabama: Field testing of MBM. *Geophysical Prospecting*, *64*(5), 1318–1334. https://doi.org/10.1111/1365-2478.12324

Dou, S., Lindsey, N., Wagner, A. M., Daley, T. M., Freifeld, B., Robertson, M., et al. (2017). Distributed acoustic sensing for seismic monitoring of the near surface: A traffic-noise interferometry case study. *Scientific Reports*, *7*(1), 11620. https://doi.org/10.1038/s41598-017-11986-4

Festa, G., Adinolfi, G. M., Caruso, A., Colombelli, S., De Landro, G., Elia, L., et al. (2021). Insights into mechanical properties of the 1980 Irpinia fault system from the analysis of a seismic sequence. *Geosciences*, *11*(1), 28. https://doi.org/10.3390/geosciences11010028

Gao, L., Xia, J., & Pan, Y. (2014). Misidentification caused by leaky surface wave in high-frequency surface wave method. *Geophysical Journal International*, *199*(3), 1452–1462. https://doi.org/10.1093/gji/ggu337

Hanks, T. C., & Kanamori, H. (1979). A moment magnitude scale. *Journal of Geophysical Research*, *84*(B5), 2348. https://doi.org/10.1029/JB084iB05p02348

Iannaccone, G., Zollo, A., Elia, L., Convertito, V., Satriano, C., Martino, C., et al. (2010). A prototype system for earthquake early-warning and alert management in southern Italy. *Bulletin of Earthquake Engineering*, *8*(5), 1105–1129. https://doi.org/10.1007/s10518-009-9131-8

Jousset, P., Reinsch, T., Ryberg, T., Blanck, H., Clarke, A., Aghayev, R., et al. (2018). Dynamic strain determination using fibre-optic cables allows imaging of seismological and structural features. *Nature Communications*, *9*(1), 2509. https://doi.org/10.1038/s41467-018-04860-y

Lindsey, N. J., Martin, E. R., Dreger, D. S., Freifeld, B., Cole, S., James, S. R., et al. (2017). Fiber-optic network observations of earthquake wavefields. *Geophysical Research Letters*, *44*(23). https://doi.org/10.1002/2017GL075722

Lior, I., Mercerat, E. D., Rivet, D., Sladen, A., & Ampuero, J.-P. (2022). Imaging an underwater basin and its resonance modes using optical fiber distributed acoustic sensing. *Seismological Research Letters*, *93*(3), 1573–1584. https://doi.org/10.1785/0220210349

Lior, I., Sladen, A., Rivet, D., Ampuero, J., Hello, Y., Becerril, C., et al. (2021). On the detection capabilities of underwater distributed acoustic sensing. *Journal of Geophysical Research: Solid Earth*, *126*(3). https://doi.org/10.1029/2020JB020925

Liu, X., Wang, C., Shang, Y., Wang, C., Zhao, W., Peng, G., & Wang, H. (2017). Distributed acoustic sensing with Michelson interferometer demodulation. *Photonic Sensors*, *7*(3), 193–198. https://doi.org/10.1007/s13320-017-0363-y

Martin, E. R., Biondi, B., Ajo-Franklin, J., & Papanicolaou, G. (2018). *Passive imaging and characterization of the subsurface with distributed acoustic sensing*. Stanford University.

Matrullo, E., De Matteis, R., Satriano, C., Amoroso, O., & Zollo, A. (2013). An improved 1-D seismic velocity model for seismological studies in the Campania–Lucania region (Southern Italy). *Geophysical Journal International*, *195*(1), 460–473. https://doi.org/10.1093/gji/ggt224

Mestayer, J., Cox, B., Wills, P., Kiyashchenko, D., Lopez, J., Costello, M., et al. (2011). Field trials of distributed acoustic sensing for geophysical monitoring. In *SEG technical program expanded abstracts 2011* (pp. 4253–4257). Society of Exploration Geophysicists. https://doi.org/10.1190/1.3628095

Papp, B., Donno, D., Martin, J. E., & Hartog, A. H. (2017). A study of the geophysical response of distributed fibre optic acoustic sensors through laboratory-scale experiments: Geophysical response of fibre optic sensors. *Geophysical Prospecting*, *65*(5), 1186–1204. https://doi.org/10.1111/1365-2478.12471

Piana Agostinetti, N., Villa, A., & Saccorotti, G. (2022). Distributed acoustic sensing as a tool for subsurface mapping and seismic event monitoring: A proof of concept. *Solid Earth*, *13*(2), 449–468. https://doi.org/10.5194/se-13-449-2022

Picozzi, M., Cotton, F., Bindi, D., Emolo, A., Maria Adinolfi, G., Spallarossa, D., & Zollo, A. (2022). Spatiotemporal evolution of ground-motion intensity at the Irpinia Near-Fault Observatory, Southern Italy. *Bulletin of the Seismological Society of America*, *112*(1), 243–261. https://doi.org/10.1785/0120210153

Rovida, A., Locati, M., Camassi, R., Lolli, B., & Gasperini, P. (2019). *Catalogo Parametrico dei Terremoti Italiani (CPTI15) versione 2.0*. Istituto Nazionale di Geofisica e Vulcanologia (INGV). https://doi.org/10.13127/CPTI/CPTI15.2

Sladen, A., Rivet, D., Ampuero, J. P., De Barros, L., Hello, Y., Calbris, G., & Lamare, P. (2019). Distributed sensing of earthquakes and ocean-solid Earth interactions on seafloor telecom cables. *Nature Communications*, *10*(1), 5777. https://doi.org/10.1038/s41467-019-13793-z

Spica, Z. J., Castellanos, J. C., Viens, L., Nishida, K., Akuhara, T., Shinohara, M., & Yamada, T. (2022). Subsurface imaging with ocean-bottom distributed acoustic sensing and water phases reverberations. *Geophysical Research Letters*, *49*(2). https://doi.org/10.1029/2021GL095287

Stabile, T. A., Satriano, C., Orefice, A., Festa, G., & Zollo, A. (2012). Anatomy of a microearthquake sequence on an active normal fault. *Scientific Reports*, *2*(1), 410. https://doi.org/10.1038/srep00410

Tromp, J., Komatitsch, D., & Liu, Q. (2008). Spectral-element and adjoint methods in seismology. *Communications in Computational Physics*, *3*(1), 1–32.

Vassallo, M., Festa, G., Bobbio, A., & Serra, M. (2016). Low shear velocity in a normal fault system imaged by ambient noise cross correlation: The case of the Irpinia fault zone, southern Italy: Passive seismic imaging of normal fault. *Journal of Geophysical Research: Solid Earth*, *121*(6), 4290–4305. https://doi.org/10.1002/2015JB012410

Wang, H. F., Zeng, X., Miller, D. E., Fratta, D., Feigl, K. L., Thurber, C. H., & Mellors, R. J. (2018). Ground motion response to an ML 4.3 earthquake using co-located distributed acoustic sensing and seismometer arrays. *Geophysical Journal International*, *213*(3), 2020–2036. https://doi.org/10.1093/gji/ggy102

Wyss, M. (1970). *Observation and interpretation of tectonic strain release mechanisms (Phd)*. California Institute of Technology. https://doi.org/10.7907/zzws-mm58

Zollo, A., Orefice, A., & Convertito, V. (2014). Source parameter scaling and radiation efficiency of microearthquakes along the Irpinia fault zone in southern Apennines, Italy. *Journal of Geophysical Research: Solid Earth*, *119*(4), 3256–3275. https://doi.org/10.1002/2013JB010116

Erratum

In the originally published version of this article, equation (3) included typographical errors involving brackets. The errors were purely typographical and the implementation of the equation was unaffected. In section 5.1, round brackets in equation 3 were changed to vertical bar. The errors have been corrected, and this may be considered the official version of record.